

# Nanopatterning of Fluorinated Graphene by Electron Beam Irradiation

Freddie Withers,<sup>†</sup> Thomas H. Bointon,<sup>†</sup> Marc Dubois,<sup>‡</sup> Saverio Russo,<sup>†</sup> and Monica F. Craciun<sup>\*,†</sup>

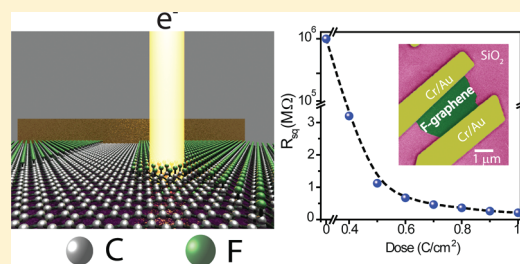
<sup>†</sup>Centre for Graphene Science, CEMPS, University of Exeter, Exeter, EX4 4QL, U.K.

<sup>‡</sup>Clermont Université, UBP, Laboratoire des Matériaux Inorganiques, CNRS-UMR 6002, 63177 Aubière, France

 Supporting Information

**ABSTRACT:** We demonstrate the possibility to selectively reduce insulating fluorinated graphene to conducting and semiconducting graphene by electron beam irradiation. Electron-irradiated fluorinated graphene microstructures show 7 orders of magnitude decrease in resistivity (from 1 T $\Omega$  to 100 k $\Omega$ ), whereas nanostructures show a transport gap in the source–drain bias voltage. In this transport gap, electrons are localized, and charge transport is dominated by variable range hopping. Our findings demonstrate a step forward to all-graphene transparent and flexible electronics.

**KEYWORDS:** Nanopatterning, fluorinated graphene, electron irradiation, electron transport



The development of flexible and transparent electronic devices relies on the availability of two types of material systems: semiconducting materials for the fabrication of active areas and highly conducting materials for use in electrical wirings.<sup>1,2</sup> Although organic molecules are promising semiconducting systems,<sup>3,4</sup> their intrinsic low carrier mobility and the large voltages usually required to operate organic devices severely limit their utility for high-speed and low-power applications.<sup>5</sup> Flexible conductors have been developed using metallic microwires<sup>6</sup> and carbon nanotubes;<sup>7</sup> however, these materials have usually limited optical transparency. Therefore, the demands for greater miniaturization, higher speed, lower power use, all embedded in a transparent device truly require novel materials.

Graphene—a single layer of carbon atoms arranged in a honeycomb structure—has a striking combination of unique properties,<sup>8–10</sup> such as an exceptionally high charge carrier mobility and conductivity,<sup>11,12</sup> while retaining excellent mechanical flexibility<sup>13</sup> and high optical transparency.<sup>14,15</sup> When functionalized with elements such as oxygen,<sup>16,17</sup> hydrogen,<sup>18,19</sup> and fluorine,<sup>20–23</sup> graphene becomes a wide gap semiconductor. This single atomic layer holds the promise for future bendable and transparent all-graphene-electronics, i.e., devices where insulating graphene is used as a host material in which conductive and semiconductive graphene channels can be opened.

Here we demonstrate a promising way toward all-graphene electronics by using fluorinated graphene as an insulating host material. We show that we can selectively reduce fluorinated graphene by electron beam irradiation and create conducting and semiconducting structures, which can be used as future electrical wirings and active device elements, respectively. We find experimentally that the relative decrease in resistance per square upon electron irradiation of microstructures is at least 7 orders of magnitude (from 1 T $\Omega$  to 100 k $\Omega$ )—3 orders of magnitude

more conductive than what was previously reported in reduced graphene oxide patterning experiments.<sup>24</sup> Further we demonstrate the nanopatterning of ribbons as narrow as 40 nm, which exhibit a transport gap in the source–drain bias voltage whose size is inversely proportional to the ribbons width. In this gap, electrons are localized, and charge transport is dominated by variable range hopping in the presence of Coulomb interactions. The demonstrated electron beam irradiation technology that we use to pattern nanochannels is easily scaled up to wafer size and it constitutes a step forward to all-graphene electronics.

The fluorination process of graphene is conducted prior to nanofabrication, by exposing natural graphite to F<sub>2</sub> atmosphere at 450 °C, resulting in a fluorine content of 28% as measured by mass uptake.<sup>25</sup> Subsequently, few-layer fluorinated graphene flakes are obtained by mechanical cleavage of fluorinated graphite onto SiO<sub>2</sub> (300 nm)/p-doped Si substrate which acts as a back gate. The flakes are then identified by their low optical contrast, typically 2–4%. Electrical contacts are fabricated by standard electron beam lithography, evaporation of Cr/Au (5 nm/70 nm), and subsequent lift-off process (see the insets of Figure 1).

To investigate the effects of electron beam irradiation on the resistivity of fluorinated graphene, we conducted an in situ electrical characterization in the scanning electron microscope vacuum chamber (<10<sup>−5</sup> mbar) by means of an electrical feedthrough. This setup preserves the flakes from any contamination by uncontrolled atmospheric dopant which can further modify the resistivity of our devices. An incident electron energy of 10 KeV and current of 0.13 nA was selected as it does not affect significantly the electronic transport properties of pristine

**Received:** June 20, 2011

**Revised:** August 10, 2011

**Published:** August 18, 2011

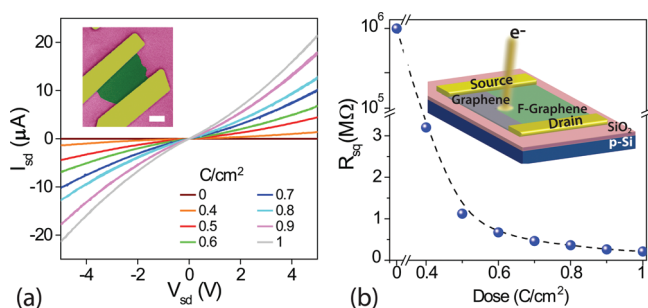


**Figure 1.** The plot in (a) shows  $I$ – $V$  characteristics for the fluorinated graphene device reported in the inset after different electron beam irradiation doses. Inset: false color SEM image of a typical fluorinated graphene device, the white bar corresponds to  $1\mu\text{m}$ . The green area corresponds to the fluorinated graphene flake, whereas the yellow parts are the Au/Cr electrodes. (b) The measured sample resistance per square plotted against the electron irradiation dose (the dashed black lines is a guideline for the eyes). The inset shows an illustration of the device configuration under irradiation with a beam of electrons.

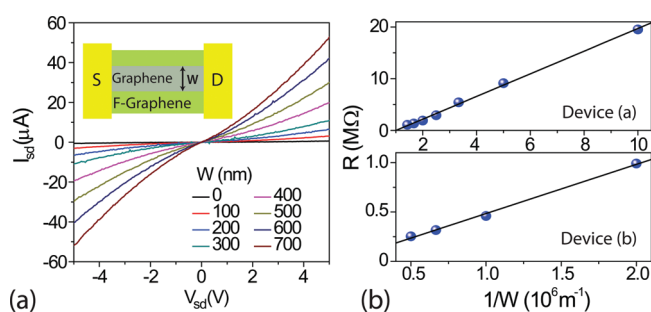


**Figure 2.** (a)  $I$ – $V$  characteristics for channels of different widths  $W$  patterned in fluorinated graphene. Graphs in (b) show the sample resistance plotted against inverse width  $W$  for two device types (see main text). The solid lines represent linear fits to the experimental data points (blue).

few-layer graphene (see Supporting Information). During the electron beam irradiation, all the electrical contacts and the back gate were connected to ground.

Figure 1a shows the evolution of the dc source–drain current versus voltage characteristics for a fluorinated graphene device after a uniform electron beam irradiation of all the flake area up to a dose of  $1\text{ C cm}^{-2}$ . It is apparent that for low doses the source–drain  $I$ – $V$  characteristics are largely nonlinear with decreasing nonlinearity for higher doses. A plot of the resistance per square ( $R_{\text{sq}}$ ) as a function of dose (see Figure 1b) summarizes the experimental finding that electron beam irradiation decreases monotonously the resistivity of fluorinated graphene, up to 7 orders of magnitude from  $1\text{ T}\Omega$  down to  $100\text{ k}\Omega$ .

To test the suitability of electron beam irradiation for patterning applications, we have performed a scaling experiment of the resistance versus width ( $W$ ) of the conductive channel. We irradiate in subsequent steps neighboring strips of  $100\text{ nm}$  width (device type a) or  $500\text{ nm}$  width (device type b) and  $1\mu\text{m}$  length, with a dose of  $1\text{ C cm}^{-2}$ . Figure 2a shows representative  $I$ – $V$  characteristics measured in situ after the progressive increase of the channel width for device (a). The resistance of the fluorinated graphene clearly decreases with increasing the number of exposed strips following a  $1/W$  dependence, for both devices (a) and (b) (see Figure 2b). These experimental findings

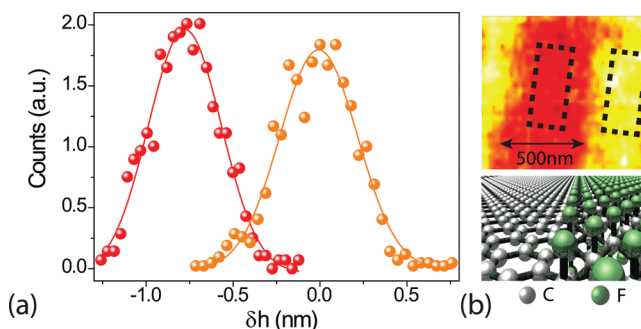


**Figure 3.** (a) AFM histogram data for the unexposed (orange) and exposed (red) fluorinated graphene extracted from the topographical AFM image shown in (b). Yellow corresponds to  $2.4\text{ nm}$  measured from the  $\text{SiO}_2$  substrate. The bottom panel in (b) illustrates the crystal structure of pristine graphene (gray) and fluorinated graphene (green).

demonstrate that irradiation opens up a conductive channel in the otherwise insulating fluorinated graphene host. Therefore, electron irradiation is well suited for patterning conductive structures on both submicrometer and micrometer scale (see also Supporting Information).

Figure 3 shows a topographical atomic force microscopy measurement of neighboring irradiated and nonirradiated fluorinated graphene regions. It is apparent that the electron irradiation does not cause any structural damage to the graphene material (see Figure 3b). However, we find a significant change in height between the irradiated and nonirradiated regions. The height of the exposed region is  $0.7\text{ nm}$  lower than the height of the unexposed region, with the latter equal to  $2.4\text{ nm}$  measured from the  $\text{SiO}_2$  (see Figure 3a). The experimentally observed reduction in height has to be expected for the electron irradiation assisted defluorination process. Indeed, previous experiments based on temperature-assisted defluorination,<sup>20</sup> demonstrated that the interatomic layer spacing between atomically flat  $\text{sp}_2$  graphene layers is smaller than the spacing between the three-dimensional atomic layers of  $\text{sp}_3$  hybridized fluorinated graphene.<sup>25</sup> The defluorination process is also consistent with the increase in the optical contrast that we observed on all the electron irradiated fluorinated graphene samples. Indeed, the closing of the large energy gap of fluorinated graphene is expected to increase the optical absorption transitions between conduction and valence bands (see Supporting Information).

The experimental observation of a significant decrease of  $R_{\text{sq}}$ , a reduction of the height, and the increase in the optical contrast of fluorinated graphene upon electron irradiation suggests that irradiation dissociates the C–F bonds, consistently with previous experimental reports on electron irradiation of graphite fluoride.<sup>26</sup> Indeed, the ionization cross section for fluorocarbons has a maximum at an electron energy of  $80\text{ eV}$ , with higher electron energies leading to progressively smaller cross sections.<sup>27</sup> Therefore, both backscattered and secondary electrons<sup>28</sup>—the latter produced by primary and backscattered electrons—have low enough energy to break the C–F bonds. However, the secondary electrons produced by backscattered electrons are unlikely to play a role in our experiments since the mean free path of backscattered electrons is larger than the typical size of the studied flakes and much larger than the mean free path of secondary electrons—just a few tens of nanometers. The electron irradiation dose of  $1\text{ C cm}^{-2}$  used in our experiments

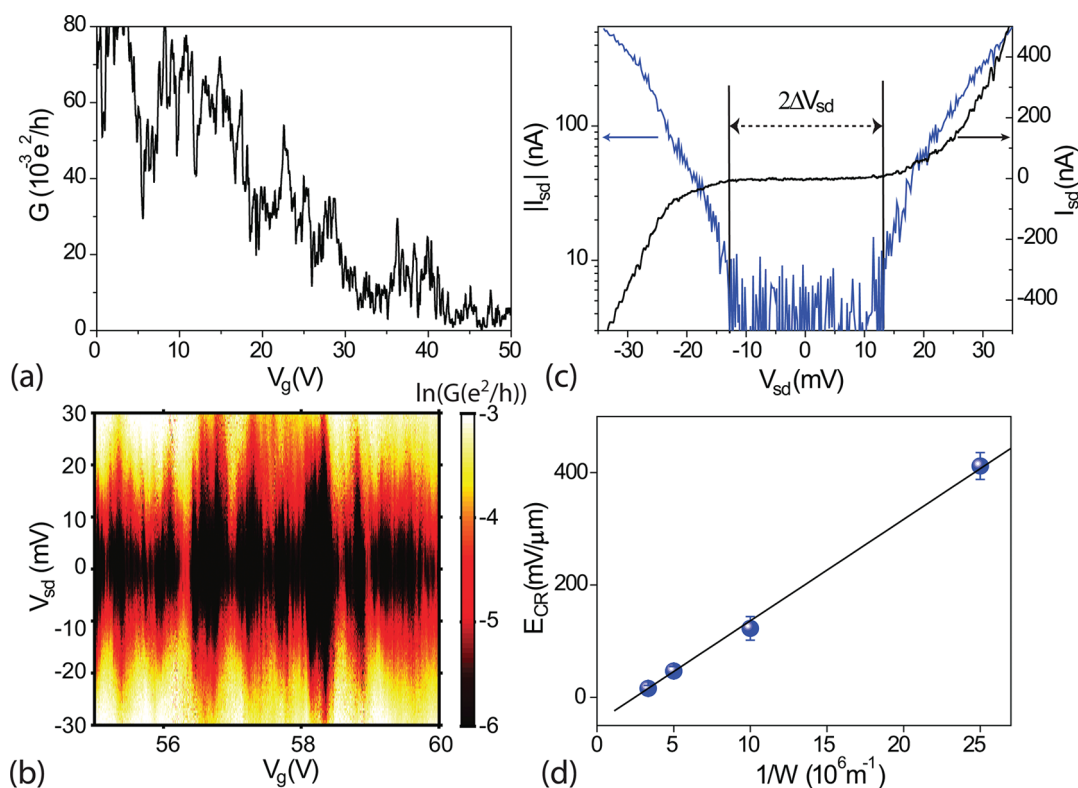


**Figure 4.** (a) Differential conductance ( $G$ ) measured with  $V_{ac} = 300 \mu\text{V}$  excitation voltage as a function of gate voltage ( $V_g$ ) for zero source–drain bias ( $V_{sd}$ ) for an electron beam irradiated nanoribbon of fluorinated graphene with width  $W = 300 \text{ nm}$  and length  $L = 1 \mu\text{m}$ . The color plot in (b) shows the evolution of  $G$  as a function of  $V_g$  and  $V_{sd}$ . (c) Plot of the source–drain current— $I_{sd}$  (black)—and the absolute value of  $I_{sd}$  (blue) as a function of  $V_{sd}$  measured at  $V_g = 55.5 \text{ V}$ , with the transport gap  $\Delta V_{sd}$  highlighted by the vertical lines. The plot in (d) summarizes the critical electric field  $E_{CR}$  versus the width of the studied nanoribbons. The solid line is a linear fit to the experimental data points (blue).

corresponds to  $6.24 \times 10^{18}$  electrons/ $\text{cm}^2$ . Since the concentration of the C–F bonds in our flakes is  $\sim 3 \times 10^{14} \text{ cm}^{-2}$  ( $\text{CF}_{0.28}$ ) with a carbon atom density of  $10^{15} \text{ cm}^{-2}$ , we can estimate the probability of the electron irradiation assisted defluorination to be  $5 \times 10^{-5}$ .

In order to probe the electronic properties of the nanostructures patterned by electron-irradiation-assisted defluorination, we have conducted electronic transport measurements over a wide temperature range (from room temperature down to 4.2 K) for nanoribbons with  $1 \mu\text{m}$  length and four different widths (300, 200, 100, and 40 nm). The devices were exposed to  $1 \text{ C cm}^{-2}$  and after exposure were annealed at a temperature of  $200^\circ\text{C}$  (much lower than the  $450^\circ\text{C}$  characteristic of the fluorination process) in 10%  $\text{H}_2/\text{Ar}$  gas for 2 h. This annealing process removes contaminants due to the electron beam irradiation while leaving the fluorinated graphene insulating. Consequently, the resistance of the electron irradiated regions approaches the typical values for pristine graphene whereas the fluorinated graphene remains insulating (see Supporting Information).

Figure 4a shows a typical plot of the zero source–drain bias ( $V_{sd} = 0$ ) differential conductance ( $G = dI_{sd}/dV_{sd}$ ) for a 300 nm wide ribbon as a function of gate voltage  $V_g$  at  $T = 4.2 \text{ K}$ . It is apparent that the electrical transport is suppressed for  $V_g > 30 \text{ V}$ , suggesting the formation of a transport gap as previously reported in etched graphene nanoribbons.<sup>29–32</sup> We observe a transport gap for all the studied ribbons whose value depends on the ribbon width (see also Supporting Information). The temperature and bias dependence of the differential conductance in

the transport gap can shed light on the origin of this gap and its relation to the level of disorder, to Coulomb interactions, and to electron confinement.

A color plot of the measured differential conductance in the transport gap region as a function of  $V_g$  and  $V_{sd}$  shows that the low bias electrical transport is suppressed (see Figure 4b for  $W = 300 \text{ nm}$  and Supporting Information for measurements on ribbons with different  $W$ ).  $G$  exhibits diamond-like structures characteristic of Coulomb blockade, indicating that electrons are confined in small regions of the nanoribbon with significant charging energy. Consistently, the  $I_{sd}$  versus  $V_{sd}$  curves measured in the transport gap are strongly nonlinear; see Figure 4c. In particular, a logarithmic scale plot of the  $I$ – $V$  characteristics highlights more clearly the presence of a source–drain bias voltage transport gap  $\Delta V_{sd}$  associated to a steep decrease of current for  $|V_{sd}| < |\Delta V_{sd}|$  (see Figure 4c). The corresponding critical electric field which has to be applied in order to activate the conduction in the disordered ribbon is therefore  $E_{CR} = \Delta V_{sd}/L$ , with  $L$  being the ribbon length.

A comparison between the conductance plots for different  $W$  reveals that the narrower the nanoribbon is, the wider is  $\Delta V_{sd}$  and the larger is  $E_{CR}$ ; see Figure 4d. These observations, combined with the fact that the Coulomb diamonds are irregular and largely overlapping, indicate that the charging regions vary in size. The dependence of  $\Delta V_{sd}$  and  $E_{CR}$  on the nanoribbon width suggests that roughness at the edges of the defluorinated ribbons contributes substantially to create localized states responsible for the transport gap.



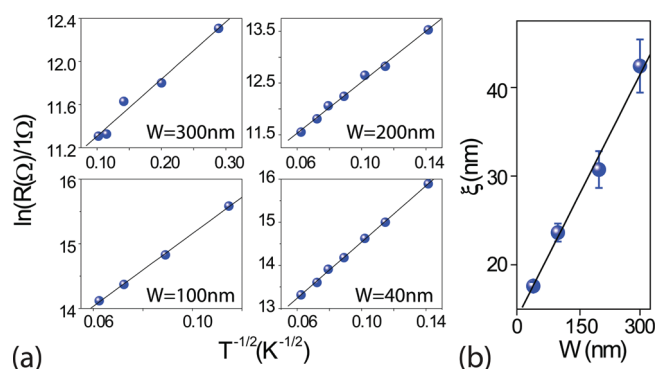


**Figure 5.** Panels in (a) show the resistance of defluorinated nanoribbons in the transport gap region plotted as a function of  $T^{-1/2}$  for different ribbons widths. The solid lines are fits to the experimental data (blue dots) to the Efros–Shklovskii variable range hopping. Panel b is a plot of the localization length  $\xi$  as a function of the nanoribbon width. The solid line represents a linear fit to the experimental data points (blue).

The role of Coulomb interactions on the electrical transport in these defluorinated nanoribbons is revealed by the temperature dependence of the conductance in the transport gap. Indeed, the logarithm of the zero bias resistivity fits well to a  $T^{-1/2}$  dependence for all the four nanoribbons widths (see Figure 5a). This functional dependence could either correspond to 1D variable range hopping (VRH) or to 2D VRH in the presence of a Coulomb gap.<sup>33,34</sup> However, for all the studied devices, the estimated diameter of the smallest charging island is always smaller than the width of the nanoribbon (see Supporting Information), indicating that electrical transport is through 2D VRH in the presence of Coulomb interactions.

The temperature dependence in the studied defluorinated nanoribbons is therefore described by the Efros–Shklovskii VRH relation:  $G = G_0 \exp(T_0/T)^{-1/2}$ , where  $T_0 = (\beta e^2)/(4\pi\epsilon_0\epsilon_r k_B \xi)$ . Figure 5b shows the estimated localization length  $\xi$  as a function of the nanoribbon width, using  $\epsilon_r = (1 + 4)/2$ . The fact that in all cases we find  $\xi \approx W$  confirms that charge transport in these defluorinated ribbons is diffusive and 2D. Furthermore, we find that  $\xi$  scales linearly with the width of the nanoribbon, which is in contrast to the width independent  $\xi$  reported in etched graphene nanoribbons.<sup>32</sup> This experimental observation suggests that, contrary to the case of etched nanoribbons, in the defluorinated ribbons both roughness at the edges and disorder in the ribbon play an equally crucial role on the electrons localization. However, more theoretical studies are required to fully understand the origin of the experimentally observed linear scaling of  $\xi(W)$ . At present, only nonlithographic techniques such as annealed nanotube-derived<sup>35</sup> and chemically derived graphene nanoribbons<sup>36</sup> have shown a low defect density and an intrinsic energy gap. Further tuning of the electron beam dose and annealing conditions will be necessary to reduce the level of disorder in the defluorinated ribbons such that these devices may be used for semiconducting applications.

In conclusion we show that the resistivity of insulating fluorinated graphene can be progressively decreased by several orders of magnitude simply by electron beam irradiation. The electron-irradiated fluorinated graphene ultimately exhibits the resistance per square of pristine graphene. We attribute the decrease in resistivity to fragmentation of C–F bonds induced by electron irradiation. Our results show that standard electron

beam patterning processes can be used to engineer conductive and semiconductive structures with sizes ranging from a few micrometers down to a few tens of nanometers. This opens up new avenues for the fabrication of graphene-based transparent and flexible electronic devices, with defluorinated graphene channels that can be used as metallic interconnects or elements of device structures. Furthermore, patterning channels with different conductivities may lead to novel resistive memory and data storage applications with multiple byte levels associated to different resistivities.

## ■ ASSOCIATED CONTENT

**S Supporting Information.** Electron irradiation of fluorinated graphene devices (investigations of other devices, gate dependence of source-drain current for the device shown in Figure 1, changes in optical contrast of fluorinated graphene upon irradiation). Electron beam irradiation of pristine few-layer graphene. Annealing effects of unexposed and exposed fluorinated graphene. Raman spectroscopy of fluorinated graphene flakes. Color plots of conductance as a function of  $V_{sd}$  and  $V_g$  for  $W = 200, 100$ , and  $40\text{ nm}$  ribbons. This material is available free of charge via the Internet at <http://pubs.acs.org>.

## ■ AUTHOR INFORMATION

### Corresponding Author

\*E-mail: M.F.Craciun@exeter.ac.uk.

## ■ ACKNOWLEDGMENT

S.R. and M.F.C. acknowledge financial support from EPSRC (Grant No. EP/G036101/1 and no. EP/J000396/1). S.R. acknowledges financial support from the Royal Society Research Grant 2010/R2 (Grant no. SH-05052). We acknowledge P. R. Wilkins for technical support.

## ■ REFERENCES

- (1) Rogers, J. A.; Someya, T.; Huang, Y. *Science* **2010**, *327*, 1603–1607.
- (2) Nomura, K.; Ohta, H.; Takagi, A.; Kamiya, T.; Hirano, M.; Hosono, H. *Nature* **2004**, *432*, 488–492.
- (3) Forrest, S. R. *Nature* **2004**, *428*, 911–918.
- (4) Facchetti, A. *Mater. Today* **2007**, *10*, 28–37.
- (5) Klauk, H. *Chem. Soc. Rev.* **2010**, *39*, 2643–2666.
- (6) Ahn, B. Y.; Duoss, E. B.; Motala, M. J.; Guo, X.; Park, S.-I.; Xiong, Y.; Yoon, J.; Nuzzo, R. G.; Rogers, J. A.; Lewis, J. A. *Science* **2009**, *321*, 1590–1593.
- (7) Sekitani, T.; Noguchi, Y.; Hata, K.; Fukushima, T.; Aida, T.; Someya, T. *Science* **2008**, *321*, 1468–1472.
- (8) Geim, A. K.; Novoselov, K. S. *Nat. Mater.* **2007**, *6*, 183–191.
- (9) Geim, A. K. *Science* **2009**, *324*, 1530–1534.
- (10) Craciun, M. F.; Russo, S.; Yamamoto, M.; Tarucha, S. *Nano Today* **2011**, *6*, 42–60.
- (11) Novoselov, K.; Geim, A.; Morozov, S.; Jiang, D.; Katsnelson, M.; Grigorieva, I.; Dubonos, S.; Firsov, A. *Nature* **2005**, *438*, 197–200.
- (12) Zhang, Y.; Tan, Y.; Stormer, H.; Kim, P. *Nature* **2005**, *438*, 201–204.
- (13) Kim, K.; Zhao, Y.; Jang, H.; Lee, S.; Kim, J.; Kim, K.; Ahn, J.; P. K.; Choi, J.; Hong, B. *Nature* **2009**, *457*, 706–710.
- (14) Nair, R.; Blake, P.; Grigorenko, A.; Novoselov, K.; Booth, T.; Stauber, T.; NMR, P.; Geim, A. *Science* **2008**, *320*, 1308–1308.
- (15) Sukang, B.; et al. *Nat. Nanotechnol.* **2010**, *5*, 574–578.

- (16) Dikin, D. A.; Stankovich, S.; Zimney, E. J.; Piner, R. D.; Dommett, G. H. B.; Evmenenko, G.; Nguyen, S. T.; Ruoff, R. S. *Nature* **2007**, *448*, 457–460.
- (17) Eda, G.; Chhowalla, M. *Adv. Mater.* **2010**, *22*, 2392–2415.
- (18) Ryu, S.; Han, M. Y.; Maultzsch, J.; Heinz, T. F.; Kim, P.; Steigerwald, M. L.; Brus, L. E. *Nano Lett.* **2008**, *8*, 4597–4602.
- (19) Elias1, D. C.; Nair, R. R.; Mohiuddin, T. M. G.; Morozov, S. V.; Blake, P.; Halsall, M. P.; Ferrari, A. C.; Boukhvalov, D. W.; Katsnelson, M. I.; Geim, A. K.; Novoselov, K. S. *Science* **2009**, *323*, 610–613.
- (20) Cheng, S.-H.; Zou, K.; Okino, F.; Gutierrez, H. R.; Gupta, A.; Shen, N.; Eklund, P. C.; Sofo, J. O.; Zhu, J. *Phys. Rev. B* **2010**, *81*, 205435.
- (21) Withers, F.; Dubois, M.; Savchenko, A. K. *Phys. Rev. B* **2010**, *82*, 073403.
- (22) Withers, F.; Russo, S.; Dubois, M.; Craciun, M. F. arXiv:1105.1751.
- (23) Nair, R. R.; et al. *Small* **2010**, *6*, 2877–2884.
- (24) Zhongqing, W.; Debin, W.; Suenne, K.; Soo-Young, K.; Yike, H.; Yakes, M. K.; Laracuent, A. R.; Zhenting, D.; Marder, S. R.; Claire, B.; King, W. P.; de Heer, W. A.; Sheehan1, P. E.; Riedo2, E. *Science* **2010**, *328*, 1373–1376.
- (25) *Fluorine-Carbon and Fluoride-Carbon Materials*; Nakajima, T., Ed.; Marcel Dekker, Inc.: New York, 1995.
- (26) Motoyama, M.; Nakajima, T.; Watanabe, N. *Solid State Ionics* **1984**, *13*, 221–225.
- (27) Bart, M.; Harland, P. W.; Hudson, J. E.; Vallance, C. *Phys. Chem. Chem. Phys.* **2001**, *3*, 800–806.
- (28) *Scanning electron microscopy and X-ray microanalysis*; Goldstein, J., Newbury, D. E., Joy, D. C., Lyman, C. E., Echlin, P., Lifshin, E., Eds.; Springer Science: New York, 2003.
- (29) Han, M. Y.; Özyilmaz, B.; Zhang, Y.; Kim, P. *Phys. Rev. Lett.* **2007**, *98*, 206805.
- (30) Han, M. Y.; Brant, J. C.; Kim, P. *Phys. Rev. Lett.* **2010**, *104*, 056801.
- (31) Gallagher, P.; Todd, K.; Goldhaber-Gordon, D. *Phys. Rev. B* **2010**, *81*, 115409.
- (32) Oostinga, J. B.; Sacepe, B.; Craciun, M. F.; Morpurgo, A. F. *Phys. Rev. B* **2010**, *81*, 193408.
- (33) Shklovskii, B. I.; Efros, A. L. *Electronic Properties of Doped Semiconductors*; Springer Series in Solid State Sciences, 45; Springer: Berlin, 1984.
- (34) *Electron-Electron Interactions in Disordered Systems*; Efros, A. L., Shklovskii, B. I., Eds.; North-Holland: Amsterdam, 1985.
- (35) Shimizu, T.; Haruyama, J.; Marcano, D. C.; Kosinkin, D. V.; Tour, J. M.; Hirose; Suenaga, K. *Nat. Nanotechnol.* **2011**, *6*, 45.
- (36) Wang, X.; Ouyang, Y.; Li, X.; Wang, H.; Guo, J.; Dai, H. *Phys. Rev. Lett.* **2008**, *100*, 206803.